2nd Advanced Optical Metrology Compendium

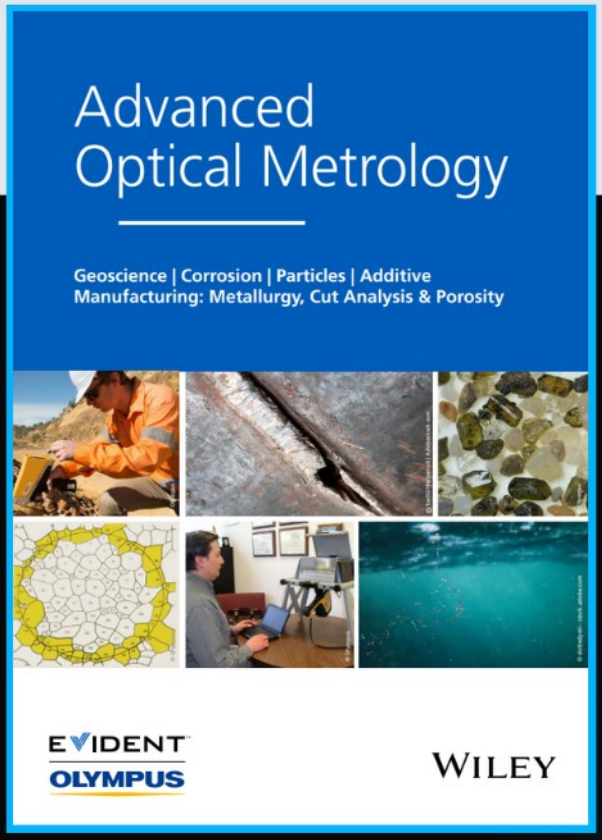

The latest eBook from Advanced Optical Metrology. Download for free.

This compendium includes a collection of optical metrology papers, a repository of teaching materials, and instructions on how to publish scientific achievements.

With the aim of improving communication between fundamental research and industrial applications in the field of optical metrology we have collected and organized existing information and made it more accessible and useful for researchers and practitioners.

EVIDENT
OLYMPUS

WILEY

ADVANCED ENGINEERING MATERIALS
www.aem-journal.com

Check for updates

Soft Pneumatic Actuators with Controllable Stiffness by Bio-Inspired Lattice Chambers and Fused Deposition Modeling 3D Printing

Mohammadreza Lalegani Dezaki, Mahdi Bodaghi, Ahmad Serjouei, Shukri Afazov, and Ali Zolfagharian*

This article shows how changing 3D printing parameters and using bio-inspired lattice chambers can engineer soft pneumatic actuators (SPAs) with different behaviors in terms of controlling tip deflection and tip force using the same input air pressure. Fused deposition modeling (FDM) is employed to 3D print soft pneumatic actuators using varioShore thermoplastic polyurethane (TPU) materials with a foaming agent. The effects of material flow and nozzle temperature parameters on the material properties and stiffness are investigated. Auxetic, columns, face-centered cubic, honeycomb, isotruss, oct vertex centroid, and square honeycomb lattices are designed to study actuators' behaviors under the same input pressure. Finite-element simulations based on the nonlinear hyper-elastic constitutive model are carried out to precisely predict the behavior, deformation, and tip force of the actuators. A closed-loop pneumatic system and sensors are developed to control the actuators. Results show that lattice designs can control the bending angle and generated force of actuators. Also, the lattices increase the ultimate strength by controlling the contact area inside the chambers. They demonstrate variable stiffness behaviors and deflections under the same pressure between 100 and 500 kPa. The proposed actuators could be instrumental in designing wearable hand rehabilitative devices that assist customized finger and wrist flexion-extension.

1. Introduction

Soft robots are created to address the limitations of traditional robots when dealing with people and delicate biological items.[1–4] Soft pneumatic actuators (SPAs) work by injecting regulated positive or negative pressure into a sealed chamber within a flexible structure. These actuators can bend, twist, extend, or shrink.[5] The actuator's reaction to applied pressure is determined by the material as well as the shape of the chambers. The actuator's geometric form or multi-material distribution can be improved in a broader sense. The autonomous design of soft actuators and robots may benefit from optimizing wall thickness and changing chamber structures. The soft actuator may produce relatively passive deformations and modify itself to the shape of an object being handled due to soft robotics' inherent compliance.[6] Hence, the chamber effects on bending and actuating are vital to enhancing the capability of the soft actuator. Also, finite element method (FEM) can be employed to improve the soft robots, predict their movements, and eliminate future issues after fabrication.[7] A wide range of novel developments has been employed to increase soft robot efficiency and many novel designs have been used to achieve the versatility and enhanced conformability of soft robotic actuators.[8–13]

Soft actuators can also provide a safer type of connection with hard bodies because of their compliance, which allows for normal joint motions during rehabilitation.[14] 3D printing of soft robots has yet to become a widespread manufacturing technology.[15] One of the most widely used 3D printing technologies in producing soft components is fused deposition modeling (FDM).[16] A wide range of soft and hard materials has been used to produce soft components and molds for commercial elastomer casting.[17,18] The most printed materials for soft robotic applications include silicone, thermoplastic polyurethane (TPU), and hydrogels. FDM enables the creation of enhanced internal features in products, as well as more control over the structure's mechanical qualities and performance.[19] For example, Yirmibesoglu et al.[20] demonstrated a bespoke

M. Lalegani Dezaki, M. Bodaghi, A. Serjouei, S. Afazov
Department of Engineering
School of Science and Technology
Nottingham Trent University
Nottingham NG11 8NS, UK
E-mail: mahdi.bodaghi@ntu.ac.uk

A. Zolfagharian
School of Engineering
Deakin University
Geelong 3216, Australia

The ORCID identification number(s) for the author(s) of this article can be found under https://doi.org/10.1002/adem.202200797.

© 2022 The Authors. Advanced Engineering Materials published by Wiley-VCH GmbH. This is an open access article under the terms of the Creative Commons Attribution License, which permits use, distribution and reproduction in any medium, provided the original work is properly cited.

DOI: 10.1002/adem.202200797

15272648, 0, Downloaded from https://onlinelibrary.wiley.com/doi/10.1002/adem.202200797 by Test, Wiley Online Library on [20/01/2023]. See the Terms and Conditions (https://onlinelibrary.wiley.com/terms-and-conditions) on Wiley Online Library for rules of use; OA articles are governed by the applicable Creative Commons License

extrusion-based 3D printer that could print silicone directly, which can be used as a soft actuator. This technique reduced the fabrication time by more than 50%.

Numerous studies propose different designs and developments using 3D printing technology.[21–23] FilaFlex material was used to print the soft monolithic fingers and gripper by Anver et al.[24] To minimize the use of supporting rafts during printing, air chambers were specifically constructed with increased lateral support. Tawk et al.[25] used a low-cost and open-source FDM and printed fingers of the soft gripper, as well as the mechanical metamaterial, which integrated a soft auxetic structure and compliant ribs. Results showed that the gripper could successfully grab a broad variety of items in three distinct configurations, including two, three, and four fingers. Yan et al.[26] proposed bio-inspired proprioception, which was innervated into a soft hand, allowing for a more robust perception of textures and object forms. With top grip and side grasp, the soft hand could detect 10 different types of items that varied in shape, with maximum accuracies of 96.33% and 96.00%, respectively. Rosalia et al.[27] presented a new form of 3D-printed soft pneumatic actuators that allowed bending modalities to be customized based on geometry. In this study, the 3D-printed SPA capable of helical motion was developed thanks to a unique feature of customizable cubes at an angle to the structure's longitudinal axis.

Ogawa et al.[28] developed a reconfigurable and vacuum-actuated soft matter modular block known as MORI-A. Depending on the 3D-printed structure contained in a unit, it achieved various uniaxial bending, shear deformation, and non-deformation behaviors. MORI-A could display elastic anisotropy depending on the density of the 3D structure it contained and the manufacturing process it followed. Ang et al.[29] described the design and preliminary testing of a completely 3D-printed soft robotic hand exoskeleton for stroke victims called a print-it-yourself (PIY) glove. Tawk et al.[30] created bio-inspired soft vacuum actuators that worked with a negative pressure. The actuators were completely 3D printed and tailored for each application. The robot was able to accomplish different tasks with 16 N force and 5.54 Hz actuation speed. Hu et al.[31] introduced a novel soft actuator that consisted of a row of internal chambers with the same helix angle that might create simultaneous bending and twisting movements. Under the same amount of input pressure, the helical actuator exhibited a higher mechanical output than the regular bending actuator (with a maximum blocking force of 1.19 N).

As the literature review shows, controlling SPAs in terms of deflection and tip force has been a challenging task when the input pressure is constant. No research work has examined the use of lattice-shaped chambers to control soft actuators' configurations. Also, in all previous research works, the capability of FDM 3D printers to control the material stiffness of actuators with the same filaments has not been studied.

This study aims to show how lattice structures inside the actuator's chambers and 3D printing parameters can control the force and bending angle. The potential of controlling the stiffness of the lattice actuators via adjusting 3D printing parameters is revealed via a set of parametric studies. It is also shown that lattice structures in the air passage can help to increase the stiffness of soft actuators in specific areas based on the requirements. Hence, a customized deflection can be achieved using lattice structures inside the chambers when the air pressure is constant. It is experimentally demonstrated that using the lattice structures can boost the final strength of actuators. The manufacturing approach allows for modifications in the actuator's design, allowing for various bending profiles to be achieved. The conceptual design and methodology presented in this study could be used for other applications such as soft robotic grippers where softness and force are important to handle brittle objects.

The followings are the article's main contributions: 1) Implementing FDM with a foaming agent varioShore TPU to design and fabricate innovative SPAs with lattice-shaped chambers in a single run. 2) Controlled and adjustable bending angle and tip force with the same input pressure for simple systems with no additional components such controllable valve and electronic board. 3) Characterization of the 3D-printed foaming agent varioShore TPUs in terms of shore hardness A. This is the first time that varioShore TPU is used to make soft actuators with various shore hardness and stiffnesses. 4) Choosing nozzle temperature and material flow parameters as control parameters to investigate their effects on the shore hardness A. 5) Development of a closed-loop control system, bending, and force sensor to control the actuator and generate data. 6) Studying the hyper-elastic properties of the varioShore TPU utilized in FDM. 7) Design and development of variable stiffness actuators bio-inspired from the natural straw. 8) Implementing FEM based on the tensile testing of 3D-printed samples to model the bending angle and the blocked force of the actuators. 9) Comparing experimental and numerical data to quantify the performance of soft actuators. 10) Investigating the ultimate strength of actuators against air pressure.

2. Experimental Section

2.1. Material Foaming Agent

The material used in this research is varioShore TPU from Colorfabb. Variable shore hardness, density, and a soft touch are all benefits of this filament. The goal is to have the softest sample which is highly important in soft robotics. Changing the nozzle temperature and material flow rate leads to adjusting the material density. Hence, investigating the material properties is vital to achieving the softest form in soft robotic actuators. Ultimaker S3 machine was used to print all specimens. Simple circular cubes with a diameter of 15 mm and a thickness of 10 mm were designed. The 3D printer parameters were constant for all specimens except material flow and nozzle temperature. The constant parameters are shown in **Table 1**. Moreover, the parameters that influence shore hardness A and density were evaluated as well. To have a comprehensive investigation of this material, 35 circular cubes were printed with different material flows and nozzle temperatures. The temperature was set from 200 to 240 °C and the flow rate was set between 60 and 120%.

Table 1. Constant printing parameters for varioShore TPU.

Parameters	Build orientation	Nozzle diameter [mm]	Filament diameter [mm]	Layer thickness [mm]	Infill density [%]	Printing pattern	Bed temp [°C]
Value	Horizontal	0.4	2.85	0.2	100	Zig Zag	0

© 2022 The Authors. Advanced Engineering Materials published by Wiley-VCH GmbH

15272648, 0, Downloaded from https://onlinelibrary.wiley.com/doi/10.1002/adem.202200797 by Test, Wiley Online Library on [20/01/2023]. See the Terms and Conditions (https://onlinelibrary.wiley.com/terms-and-conditions) on Wiley Online Library for rules of use; OA articles are governed by the applicable Creative Commons License

A manual Sauter HB analogue shore hardness tester was used to measure the shore hardness A of 3D-printed specimens followed by ASTM D2240. The value of shore hardness A was between 0 and 100.

2.2. Hyper-Elastic Constitutive Models

A uniaxial tensile test was utilized to obtain the varioShore TPU's stress–strain relationship to examine its behavior. To test the influence of alternative nozzle temperatures and material flows on the material behavior, the parameters which achieve the softest samples were chosen for printing dog-bone samples. In this case, three samples with 60% material flow and 220 °C were printed using a longitudinal infill pattern. The tests were carried out on samples in accordance with ASTM D638, with all the samples being stretched at a rate of 5 mm min^{-1} using an electromechanical Shimadzu AG-X plus machine, and TRViewX recorded the data accordingly. This test was carried out in a single 3D printing orientation since the stress–strain curves of longitudinal and transverse directions have similar trends in all orientations.[32]

Figure 1a shows the sample size and Figure 1b illustrates the average stress–strain chart of 3D-printed dog-bone samples. The constitutive model fitting was examined for the material printed in the longitudinal orientation since the bulk of the stresses occurred in the longitudinal direction during actuation. **Table 2** summarizes the strain energy equation for each hyper-elastic model. The parameter values derived for the strain energy function are reported in **Table 3**. For modest strains (less than 50%), the Neo-Hookean model demonstrated good agreement. The Yeoh model captured elastic behavior accurately across a wide range of strains and can predict stress–stretch behavior in various deformation modes using data obtained from simple uniaxial testing. The average longitudinal data was fitted to Yeoh's hyper-elastic model. The experimental data from mechanical testing in the strain range of 0-5 was fitted using this model.[33]

Table 3. Parameter values for four hyper-elastic models.

Model	Parameter value	
Neo-Hookean	μ	2.9554
Mooney–Rivlin	C_{10}	0.87897
	C_{01}	1.634
Yeoh	C_{10}	2.038
	C_{20}	0.039
	C_{30}	0.00057
Ogden	μ_1	7.623e-05
	α_1	7.5277
	μ_2	7.6286e-05
	α_2	7.5293
	μ_3	7.6287e-05
	α_3	7.5281

2.3. Bio-Inspired Design

The initial stage in the design process was to create the 3D computer-aided design (CAD) models of the soft actuators. Actuators having lattices inside the chambers were more

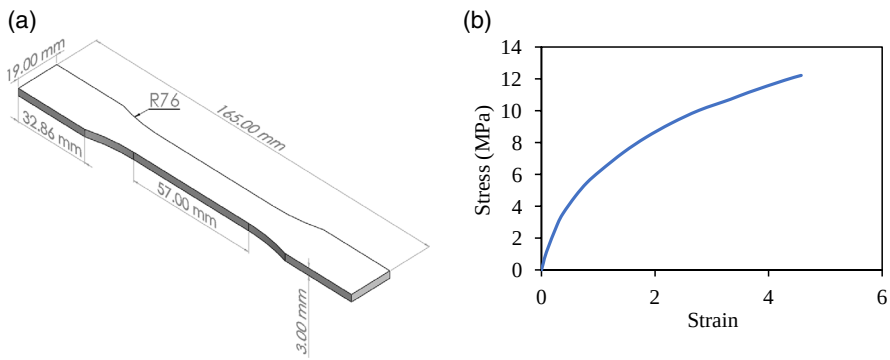

Figure 1. a) 3D modeling of dog-bone shape sample. b) Average stress–strain curve of tested 3D-printed varioShore thermoplastic polyurethane (TPU).

Table 2. The strain energy function of hyper-elastic models.[34]

Model	Strain energy equation
Neo-Hookean	$W = C_1(I_1 - 3) = \frac{\mu}{2}(I_1 - 3)$
	μ is the shear modulus, $I_1 = \lambda_1^2 + \lambda_2^2 + \lambda_3^2$ is a principal invariant, and $\lambda_i = l_i/L_i\lambda_1^2$ is the ratio of deformed length l_i to undeformed length L_i
Mooney–Rivlin	$W = C_{10}(I_1 - 3) + C_{01}(I_2 - 3)$
	C_{10}, C_{01} are material-specific parameters, while I_1, I_2 are the first and second deviatoric strain invariants
Yeoh	$W = C_{10}(I_1 - 3) + C_{20}(I_1 - 3)^2 + C_{30}(I_1 - 3)^3$
	C_{10}, C_{20}, and C_{30} are material-specific parameters, while I_1 is the first deviatoric strain invariant
Ogden	$W = \sum_{i=1}^{3} \frac{\mu_i}{\alpha_i}(\lambda_1^{\alpha_i} + \lambda_2^{\alpha_i} + \lambda_3^{\alpha_i} - 3)$
	λ_1, λ_2, and λ_3 are deviatoric major stretches, whereas μ_i and α_i are empirical parameters

© 2022 The Authors. Advanced Engineering Materials published by Wiley-VCH GmbH

15272648, 0, Downloaded from https://onlinelibrary.wiley.com/doi/10.1002/adem.202200797 by Test, Wiley Online Library on [20/01/2023]. See the Terms and Conditions (https://onlinelibrary.wiley.com/terms-and-conditions) on Wiley Online Library for rules of use; OA articles are governed by the applicable Creative Commons License

challenging to design and produce than hollow actuators. Lattice shape-chambered design inspired by the natural straws was suggested in this article to have adjustable 3D-printed pneumatic actuators (see **Figure 2**a). The internal structure of natural straw was covered by lattice structures. This bio-inspired design allowed for variable stiffness actuators in a single system using a constant air supply instead of using different moduli. The bio-inspiration from the natural straw aided in developing lattice structures inside the chambers to achieve variable stiffness actuators.[35]

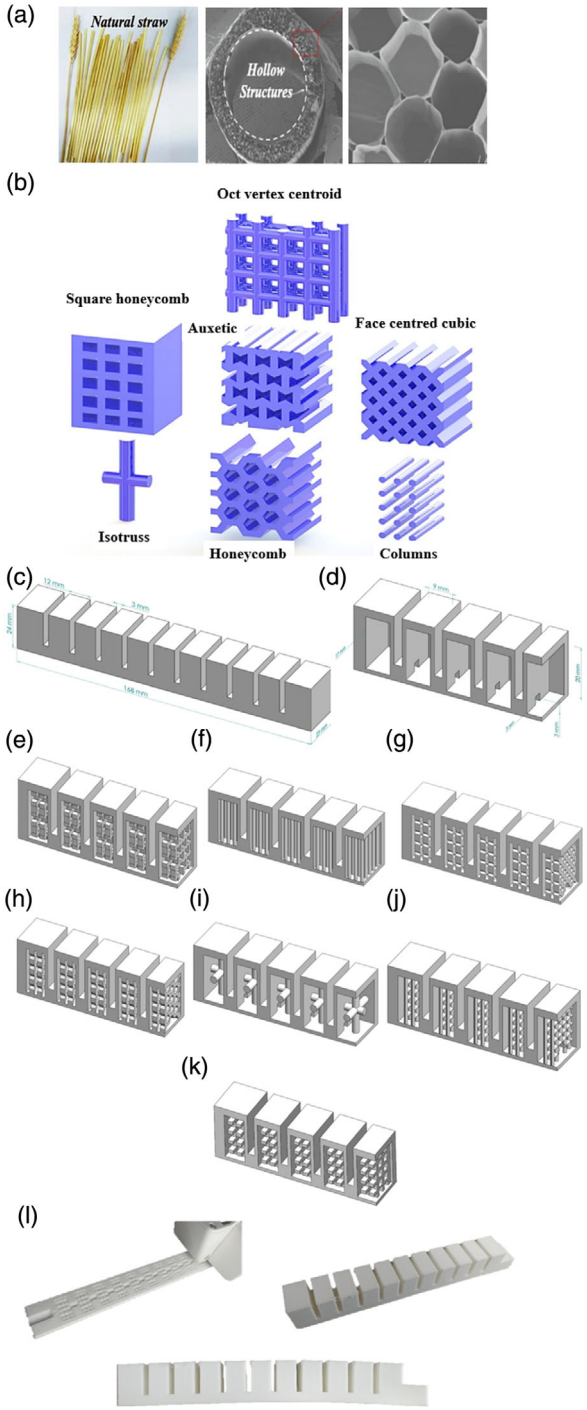

Figure 2. a) Natural straw with microstructure view.[36] 3D modeling of: b) lattice structures, c) base-design actuator, d) chambers' sizes, e) auxetic, f) columns, g) face-centered cubic, h) honeycomb, i) isotruss, j) oct vertex centroid, and k) square honeycomb structures for SPAs. l) 3D-printed soft TPU actuators.

The base design of the actuators was designed in SolidWorks software as shown in Figure 2b. Auxetic, columns, face-centered cubic, honeycomb, isotruss, oct vertex centroid, and square honeycomb lattice structures were used in this study. Their designs were modified to be implemented inside the chambers (see Figure 2c). The dimensions of the chambers are shown in Figure 2d. Seven lattice structures were designed and assigned to the chambers to find out their effects on actuators' behavior, as shown in Figure 2e–k. To increase the precision of the actuator manipulation inside their respective workspaces, a higher number of cavities can be utilized. In this case, 11 chambers were used to achieve better results. Hence, the actuator design was determined by the application and performance. The number of separate pneumatic sources or simultaneous controllers employed in the pneumatic system was considered when choosing an actuator design.

The samples were meant to be 3D printed without the usage of support materials or postprocessing techniques. Cura software was used to slice the models. The SPAs were 3D printed using varioShore TPU utilizing Ultimaker S3 FDM 3D printer. The slicer was used to modify the 3D printing parameters to 3D print entirely airtight, dependable, and functioning SPAs. The optimum printing parameters are shown in **Table 4**. To reduce the amount of material needed during 3D printing, additional support settings were not used. The process took around 30 h to print all actuators. An example of a 3D-printed sample is shown in Figure 2l.

The actuators with a sidewall thickness of 2 mm were found to be airtight in this study. As a result, it was recommended that sidewall thickness should be at least 1 mm. The size of all actuators was constant and similar. To accommodate lattice structures inside chambers, the actuators were scaled up to achieve accurate results. A simple chamber with a hole was developed to fix the air inlet pipe and the actuator during testing as shown in Figure 2l. Also, the thickness of lattice structures should be at least 1 mm to avoid material drop or poor binding. No postprocessing and support structures were required for the actuators generated in this investigation. When the actuator was fabricated, it was obvious that gravity plays a significant role in its bending ability. The FEM and experimental methods were used to accommodate this.

Table 4. Printing parameters for SPAs.

Printing parameters	Value
Build orientation	Horizontal
Nozzle diameter [mm]	0.4
Filament diameter [mm]	2.85
Layer thickness [mm]	0.2
Infill density [%]	100
Printing pattern	Linear
Material flow [%]	100
Nozzle temp. [°C]	220
Bed temp. [°C]	0

© 2022 The Authors. Advanced Engineering Materials published by Wiley-VCH GmbH

15272648, 0, Downloaded from https://onlinelibrary.wiley.com/doi/10.1002/adem.202200797 by Test, Wiley Online Library on [20/01/2023]. See the Terms and Conditions (https://onlinelibrary.wiley.com/terms-and-conditions) on Wiley Online Library for rules of use; OA articles are governed by the applicable Creative Commons License

The model was simulated for gravity and pressure after a steady state situation is attained. The actuator was fixed at its base and modeled horizontally to consider the gravitational influence.

2.4. Air and Motion Control

A Clarke air compressor with an 8-bar maximum working pressure was used to actuate the soft actuators. A simple air pressure gauge was used to control the amount of air coming to the actuator. An electronic board was developed to control the airflow accordingly. An open-source Arduino board was used to program the system. An electro-pneumatic solenoid valve (5/2) was used to control the input air supply. Since the TPU material was tougher compared to the silicone and the size of the actuators is large, the used pressure in this study was from 2 to 6 bar to investigate the soft actuators bending with various applied pressures. An electrical 5 V relay switch was used to turn off and turn on the solenoid valve. As soon as the actuator achieved the highest bending, the relay switched off the air outlet of the solenoid valve. The schematic of the system is shown in **Figure 3**. The motion of the actuator was captured using a video camera, and the bending angles were measured with a bending resistive sensor. The actuators were horizontally clamped, and data were recorded simultaneously during the procedure. A force-sensing resistor (FSR) was also used to measure the generated force by each actuator. The force sensor was calibrated using the voltage divider technique to achieve accurate results in terms of the actuator's force. The resistance of the force sensor was measured using various weights, as shown in **Figure 4**a. By increasing the weight, the sensor's resistance was decreased gradually. Hence, the output voltage was calculated by $V_{\mathrm{OUT}} = V_{\mathrm{IN}} \frac{R_{\mathrm{M}}}{R_{\mathrm{M}}+R_{\mathrm{FSR}}}$, as shown in Figure 4b. This calibration was used to measure the blocked force of each actuator. Also, Kinova software was used to capture the motion and provide the trajectory path of soft actuators.

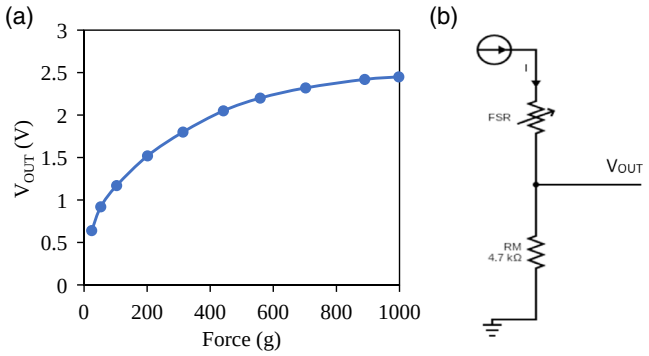

Figure 4. a) Output voltage and force curve of the force-sensing resistor (FSR) sensor. b) A schematic of output voltage to calculate the generated force.

2.5. FEM of Soft Robotic Actuator

The simulation added value to the research since the digital model can be used for further digital designs without any need for manufacturing and experimentation. The stress–-strain data from the tensile test were used in the simulation. The data were loaded into the ABAQUS/CAE (Simulia, Dassault Systemes, RI) software. The material model was produced to simulate the soft actuators, predict their behavior, and enhance their performance. The simulation was repeated until the required performance was attained, which can be compared with 3D-printed actuators. The simulations were carried out with a static analysis. ABAQUS was suited for static structural simulations employing hyper-elastic materials. An adaptive mesh with higher order tetrahedral

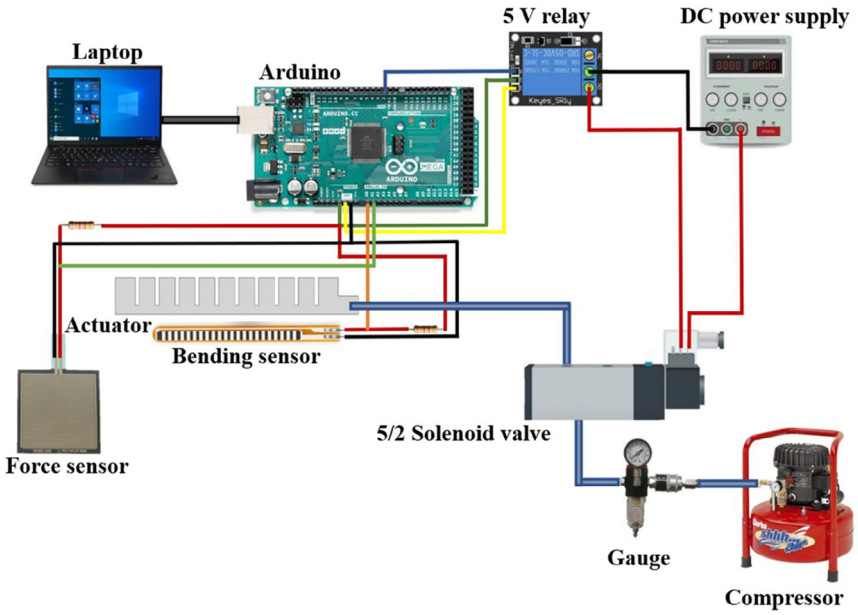

Figure 3. A schematic of the air control system with force and bending sensor.

© 2022 The Authors. Advanced Engineering Materials published by Wiley-VCH GmbH

15272648, 0, Downloaded from https://onlinelibrary.wiley.com/doi/10.1002/adem.202200797 by Test, Wiley Online Library on [20/01/2023]. See the Terms and Conditions (https://onlinelibrary.wiley.com/terms-and-conditions) on Wiley Online Library for rules of use; OA articles are governed by the applicable Creative Commons License

elements was used to mesh the models of the soft actuators. It was assumed that the material is isotropic and incompressible. A sizing function was used when a mesh with a certain element size was required. The actuator's material has hyperelastic characteristics and a density of 1.2 g cm^{-3}.

Tetrahedron meshes employed were acceptable for hyperelastic materials. An extremely fine mesh was not suggested since such actuators can experience substantial deformations. Convergence required a mesh that is quite coarse. The mesh size was chosen with care to ensure that the solution is not reliant on it. All surfaces that come into contact during deformation were characterized as frictional self-contact pairs. The contacts' behavior is changed to be symmetric to minimize penetration, producing more accurate results and realistic behavior. A pressure of up to 500 kPa was applied to the internal surfaces of their hollow chambers and a fixed support boundary condition was applied to their base. Gravity was also assigned to achieve accurate results. Solid tetrahedral quadratic hybrid elements were used to simulate all the actuators' components (ABAQUS element type C3D10H). The actuators' proximal ends were subjected to the ENCASTRE boundary condition. The inlets of the actuators were ignored for computational efficiency, and air pressure was delivered directly to all the interior cavity walls.

3. Results and Discussions

3.1. Material Shore Hardness

A few specimens failed during the printing due to the non-optimized 3D printing parameters. The shore hardness A values are recorded in **Table 5**. The Taguchi method is implemented using Minitab software to find out the effects of nozzle temperature and material flow rate on the shore hardness. It is also used to optimize the printing parameters in terms of achieving the softest 3D-printed samples. The input variables are material flow and nozzle temperature, and the output is shore hardness.

Table 5. The variable 3D printing parameters of circular cubes.

Sample [#]	Flow [%]	Temp. [°C]	Shore hardness	Sample [#]	Flow [%]	Temp. [°C]	Shore hardness
1	60	200	65	19	90	230	70
2	60	210	64	20	90	240	Failed
3	60	220	63	21	100	200	65
4	60	230	65	22	100	210	64
5	60	240	67	23	100	220	65
6	70	200	71	24	100	230	67
7	70	210	76	25	100	240	68
8	70	220	77	26	110	200	Failed
9	70	230	78	27	110	210	Failed
10	70	240	Failed	28	110	220	67
11	80	200	67	29	110	230	69
12	80	210	70	30	110	240	71
13	80	220	74	31	120	200	Failed
14	80	230	78	32	120	210	Failed
15	80	240	Failed	33	120	220	67
16	90	200	Failed	34	120	230	68
17	90	210	64	35	120	240	74
18	90	220	65	–	–	–	–

The material expands to around 1.4–1.6 times its original volume at temperatures between 200 and 240 °C. The samples are printed without foaming property between 190 and 200 °C, resulting in distinct haptics and tougher prints than foamed samples. This means the greater the temperature, the more CO_2 gas is produced, leading to the softest 3D-printed objects. The size and number of bubbles grow as the printing temperature is raised. The foaming agent increases the volume and decreases the density.[37] The flow rate should be adjusted in accordance with the printing temperature to offer excellent adhesion and connection between printing layers since the material density and printing temperature are related. The value of shore hardness fluctuates between 60 and 78 accordingly.

The Taguchi method indicates that the optimum parameters to print the softest TPU samples are a 60% flow rate and a 220 °C nozzle temperature. **Figure 5**a shows the mean material flow rate using the Taguchi method. The smaller value leads to a lower hardness. The lowest shore hardness A value of 63 is achieved. As shown in Figure 5b, the data is analyzed using MATLAB to show the lowest value of hardness as well as the optimum parameters. The optimum parameters to print TPU material are the low flow rate and average nozzle temperature. The lowest shore hardness is achieved when the flow rate is the lowest. The nozzle temperature should be set between 210 and 220 °C to achieve the lowest hardness. Also, choosing 60% of the flow rate results in low hardness due to the optimum time of material deposition and enough time for the melted material to expand its original volume. In brief, 60% of material flow rate and 220 °C are the optimum printing parameters to print varioShore TPU.

3.2. Bending Curvature

The soft actuators are controlled by varying the air pressure. The actuators bend when air pressure is applied to them. The compressor powers the pneumatic actuator. The actuator manufactured by varioShore TPU produces a range of bending degrees depending on the test. **Figure 6**a,b shows the simple actuator's bending in simulation and experiment. The applied pressure is from 100 to 500 kPa for all actuators. Figure 6c illustrates the trajectory path of actuators with different values of pressure. In the FEM simulations, identical bending angles are clearly observed. Figure 6d shows how closely the simulated and experimental findings coincide at various applied pressures. With a maximum difference of 3.15% at 300 kPa and a minimum difference of 0.6% at 200 kPa, it is found that the FEM models can accurately match the observed bending angles.

As demonstrated in **Figure 7**a,b, there appears to be a 5° to 10° difference between modeling and experimental data for a simple actuator. The lattice-shaped actuators show slightly different behaviors. The lattice structures inside the chambers avoid the structure bending completely. The structures inside the chambers do not allow them to fully expand. Figure 7c,d illustrates the isotruss deformation using 200 and 500 kPa pressure. This is the reason that the actuator cannot bend like a simple

© 2022 The Authors. Advanced Engineering Materials published by Wiley-VCH GmbH

15272648, 0, Downloaded from https://onlinelibrary.wiley.com/doi/10.1002/adem.202200797 by Test, Wiley Online Library on [20/01/2023]. See the Terms and Conditions (https://onlinelibrary.wiley.com/terms-and-conditions) on Wiley Online Library for rules of use; OA articles are governed by the applicable Creative Commons License

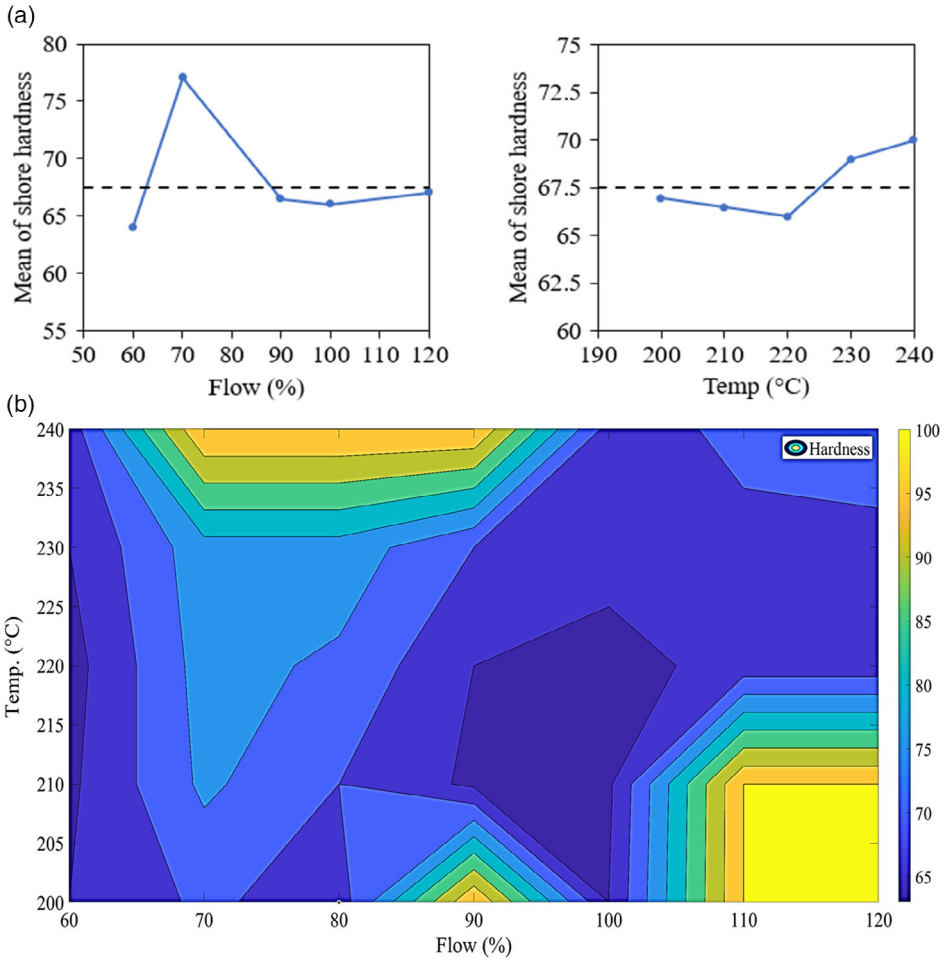

Figure 5. Results of the Taguchi method for the material flow and nozzle temperature in terms of: a) mean values for shore hardness. b) Contour plot of the value of shore hardness with different values of the flow rate and temperature.

actuator. Also, by increasing the pressure, the bending is not following a linear trend. Results indicate that isotruss actuator has a higher bending compared to other actuators except for the simple one. An adjustable bending angle is achieved using these novel soft actuators.

The projected bending angle in the simulation is thus greater than the observation. That is due to the fact that the simulation is done in reasonably perfect actuators[38] and some pressure losses, such as those in the pneumatic network and accompanying pipes, are not incorporated into the simulation. Also, the actuator is incapable of fully recovering its initial shape upon releasing air. The experimental bending angle is not exactly 0° as predicted when air pressure is removed. This might be due to the soft TPU's characteristics, gravity, and very low plasticity. This small difference could be simulated by implementing a FEM with more advanced material models and taking into account geometrical/material imperfections due to the 3D printing.[25] The actuators with different lattice structures are tested, and the bending angles under the same pressure are compared. Three measurements are taken for each sample, and the average value is chosen as the result.

The honeycomb and face-centered cube actuators have the minimum bending angle. The isotruss specimen shows a higher bending angle compared to other lattice structures. The optimum design is chosen based on the requirements. The honeycomb structure can be used as a soft actuator where the lowest bending is required. Meanwhile, isotruss shows a better performance in terms of higher bending. In brief, lattice structures improve the stiffness and strength as well as control bending angle without additional parts. This helps to control the actuator and customize the bending angle using a constant air pressure. Also, a combination of lattice structures leads to a better control capability and results in a system with adjustable deformation.

3.3. Blocked Force Measurement

The blocked force is an essential performance parameter for soft actuators. It is the force produced by the soft actuator's tip and shows the actuator's ability to transfer pressure to force. The actuator is fastened at one end to operate as a cantilever beam. The output force rises as the input pressure increases. When the force is measured, the pressure is increased by

© 2022 The Authors. Advanced Engineering Materials published by Wiley-VCH GmbH

15272648, 0, Downloaded from https://onlinelibrary.wiley.com/doi/10.1002/adem.202200797 by Test, Wiley Online Library on [20/01/2023]. See the Terms and Conditions (https://onlinelibrary.wiley.com/terms-and-conditions) on Wiley Online Library for rules of use; OA articles are governed by the applicable Creative Commons License

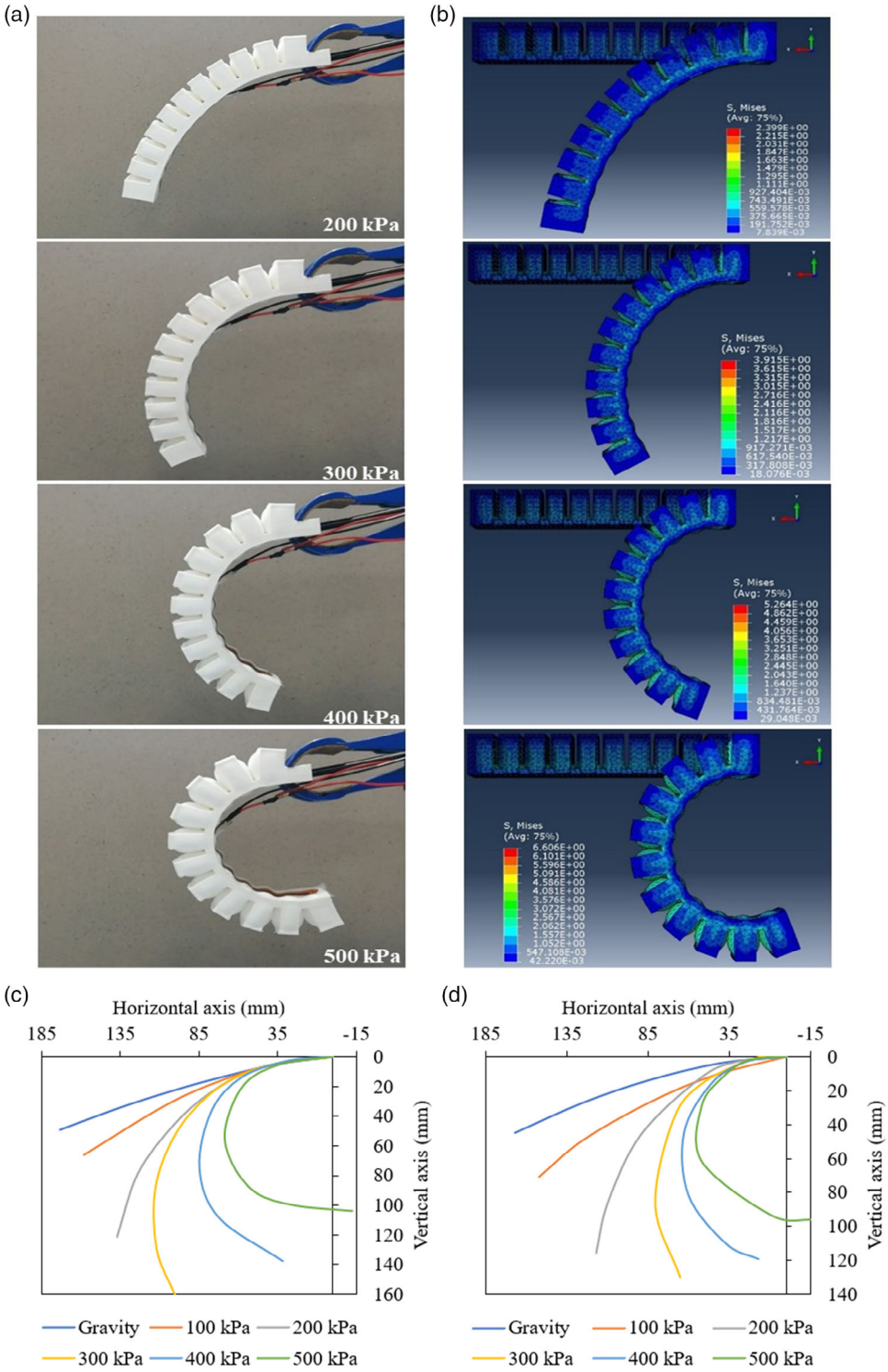

Figure 6. A comparison of simple actuator bending shape in: a) experiment and b) simulation with 200, 300, 400, and 500 kPa pressure. Bending trajectory of: c) experiment and d) simulation for actuators without an internal lattice.

100 kPa steps to a maximum pressure of 500 kPa. The bending angle is minimal when just a small amount of pressure is applied to the actuator, and the blocked force is mostly generated by the actuator's weight. When the input pressure is high enough, the sensor provides resistance to the actuator's bending actions. When the actuator meets the sensor base, it bends into an arch

 © 2022 The Authors. Advanced Engineering Materials published by Wiley-VCH GmbH

15272648, 0, Downloaded from https://onlinelibrary.wiley.com/doi/10.1002/adem.202200797 by Test, Wiley Online Library on [20/01/2023]. See the Terms and Conditions (https://onlinelibrary.wiley.com/terms-and-conditions) on Wiley Online Library for rules of use; OA articles are governed by the applicable Creative Commons License

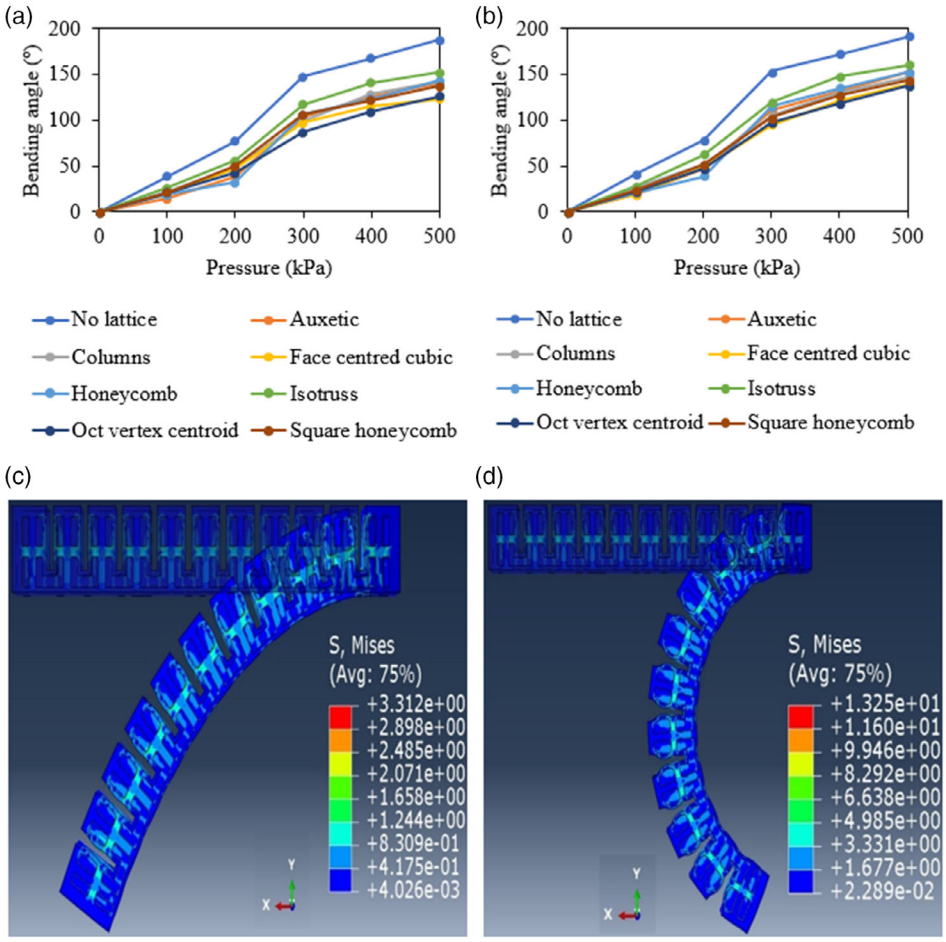

Figure 7. a) Experimental and b) numerical bending angle results for different lattice structures. Deformation of isotruss actuator using: c) 200 kPa and d) 500 kPa pressure.

(see **Figure 8**a). The top layer of the actuator expands and slides forward when inflated. The increased blockage can be due to the bending motions and sensor contact.

Moreover, fixed support is allocated to the proximal end of the actuator for the blocked force simulations in ABAQUS, which functions as a cantilever beam. The distal end of the actuator slides friction-free across the displacement support, mimicking the load cell, allowing force measurements to be taken (see Figure 8b).[39] As a result of the displacement support resisting the soft actuator's bending deformation during pressurization, the actuator bends backward in an arch and slides over the displacement support. Figure 8c,d summarizes blocked force data for actuators. With a higher pressure, the actuator force increases as well.

At 500 kPa, the highest force and actuation pressure measured for the actuator without lattice is 2.5 N. The difference between simulation and force is 0.05 N, which shows that the simulation can predict the blocked force. The 3D-printed actuators can sustain a high pressure and create a larger force. In general, an actuator without a lattice structure allows for higher pressure input, resulting in bigger blocked forces. Actuators with bio-inspired lattice-shaped chambers show lower blocked force compared to simple one. This occurs due to the structures inside the chambers, which avoid a full deformation. This means controllable soft actuators can be achieved without additional parts. Required force can be accomplished using this technique to eliminate extra effort. The bending and tip force results of the actuator without lattice-shaped chambers are similar to the previous research works.[25,39–41] This means the actuator works properly and achieved the required results with varioShore TPU material. However, implementing lattice structures inside the chambers results in controlling the bending and tip force of the pneumatic actuators accordingly.

3.4. Ultimate Strength

The actuators are put through a continuous testing to see how long they can last. The time the actuator can tolerate before failing is determined. 600 kPa actuation pressure is chosen that is higher than the pressure that the actuator can accomplish in a complete bending motion and bears. The maximum time that the actuator without lattice is tolerated is shown in **Figure 9**. The air begins to flow from the actuator once that pressure is reached, and the actuator's wall finally breaks. It can clearly

© 2022 The Authors. Advanced Engineering Materials published by Wiley-VCH GmbH

15272648, 0, Downloaded from https://onlinelibrary.wiley.com/doi/10.1002/adem.202200797 by Test, Wiley Online Library on [20/01/2023]. See the Terms and Conditions (https://onlinelibrary.wiley.com/terms-and-conditions) on Wiley Online Library for rules of use; OA articles are governed by the applicable Creative Commons License

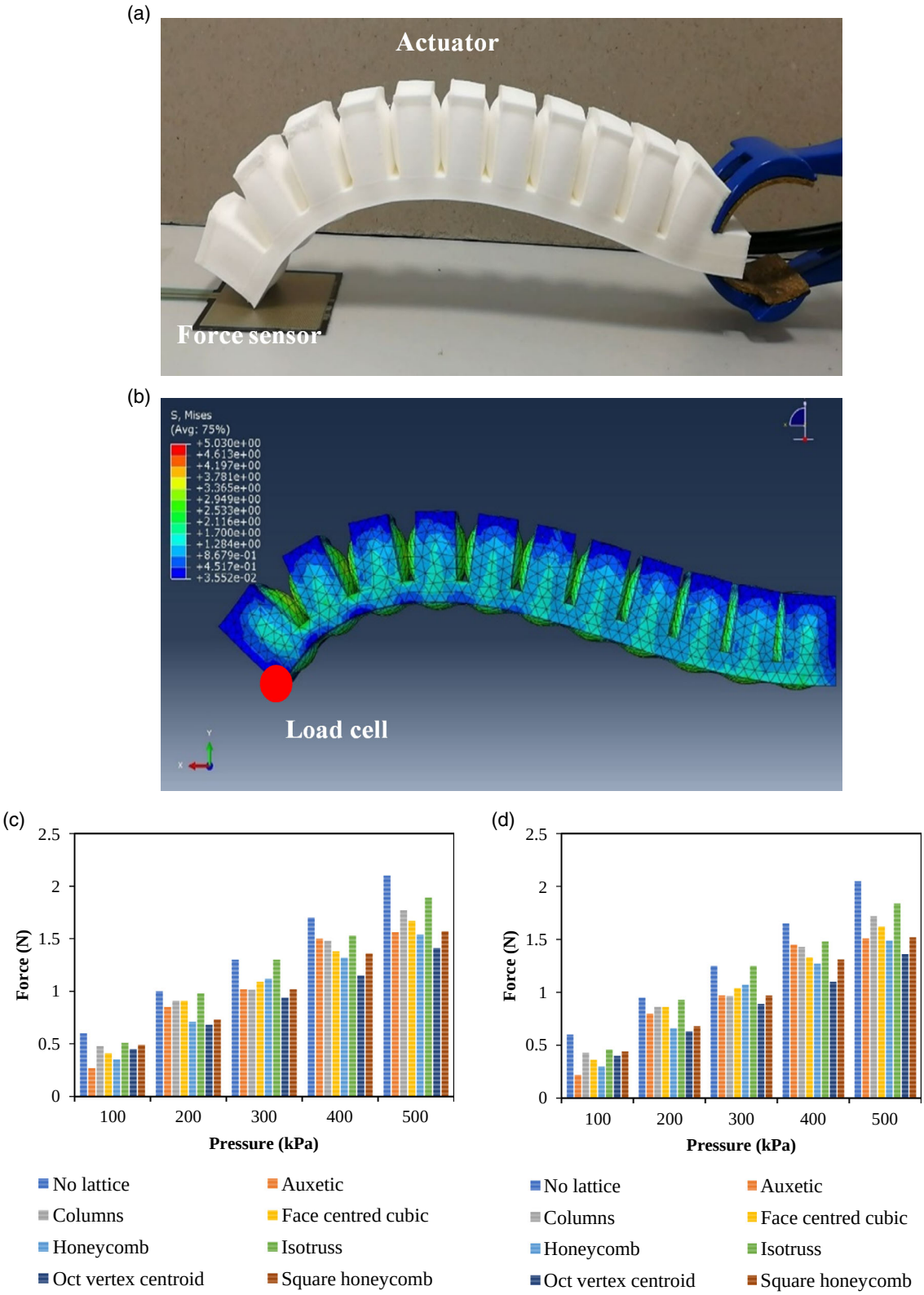

Figure 8. a) Experiment and b) simulation for blocked force measurements using a pressure of 500 kPa. The blocked force values for actuators in: c) experimental and d) simulation measurement.

© 2022 The Authors. Advanced Engineering Materials published by Wiley-VCH GmbH

15272648, 0, Downloaded from https://onlinelibrary.wiley.com/doi/10.1002/adem.202200797 by Test, Wiley Online Library on [20/01/2023]. See the Terms and Conditions (https://onlinelibrary.wiley.com/terms-and-conditions) on Wiley Online Library for rules of use; OA articles are governed by the applicable Creative Commons License

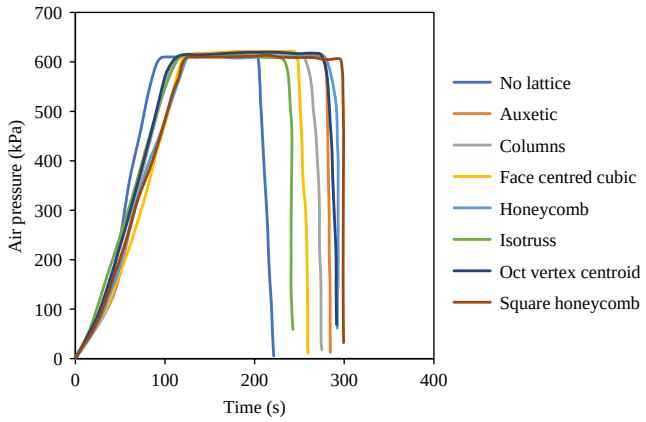

Figure 9. The maximum failure time and ultimate strength of actuators using 600 kPa air pressure.

be seen that the actuators with bio-inspired lattice shape chambers stand more compared to the sample without lattice. The actuator without a lattice structure stands at 200 s while the square honeycomb stands at 296 s. The results indicate the lattice structure inside chambers increases the strength of walls. The wall cannot expand completely, thus, the chambers withstand more pressure. In this case, isotruss actuator shows better behavior compared to the actuator without lattice. However, the ultimate strength of isotruss actuator is higher which helps to increase the lifetime of SPAs.

3.5. Application Concept

One of the 3D-printed actuators' usefulness is in wearable soft robotic applications.[42–44] SPAs have been found to offer great qualities for assistive and rehabilitative robotics in helping, augmenting, and restoring patient movement for motor rehabilitation in previous studies.[45–47] SPAs are more compliant than rigid pneumatic actuators because they are built of materials with elastic moduli that are compatible with human tissues. However, the material should be firm enough to give an adjustable bending angle and blocking force to complete the required tasks. As a result, the wearer's risk of pain and injury would considerably be decreased. **Figure 10** illustrates a 3D schematic of developed actuators as assistive devices to illustrate a potential application of our 3D-printed actuators. The uniqueness of these actuators compared to previous ones is in their conceptual design and manufacturing. In terms of bending angle and produced force, actuators having lattice chambers behave differently from basic actuators without lattice. Using lattice structures inside SPAs can help to have a better flexibility with just one input pressure. The weight of the five actuators is 135.27 g.

The generated force and bending angle of the proposed actuators are within the range reported for previous SPAs.[32,38,40,41,48] The proposed actuators can mimic the function of the human hand due to the variable stiffness and behavior. Also, this technique eliminates using various pneumatic parts to have an adjustable bending in actuators. Meanwhile, using a lattice design in SPAs brings adjustable bending to each finger. Also, by combining the lattice structures into one actuator, it would be possible to control the bending using the same pressure without additional devices. This research enables to have various bendings in specific areas. Having different lattices in each block of actuators could produce different stiffness and bending functions compatible with the joint's motions between three parts of the human finger bones, namely proximal, middle, and distal phalanges. Also, the actuators could be able to aid finger flexion as well as wrist flexion due to the variable stiffness.

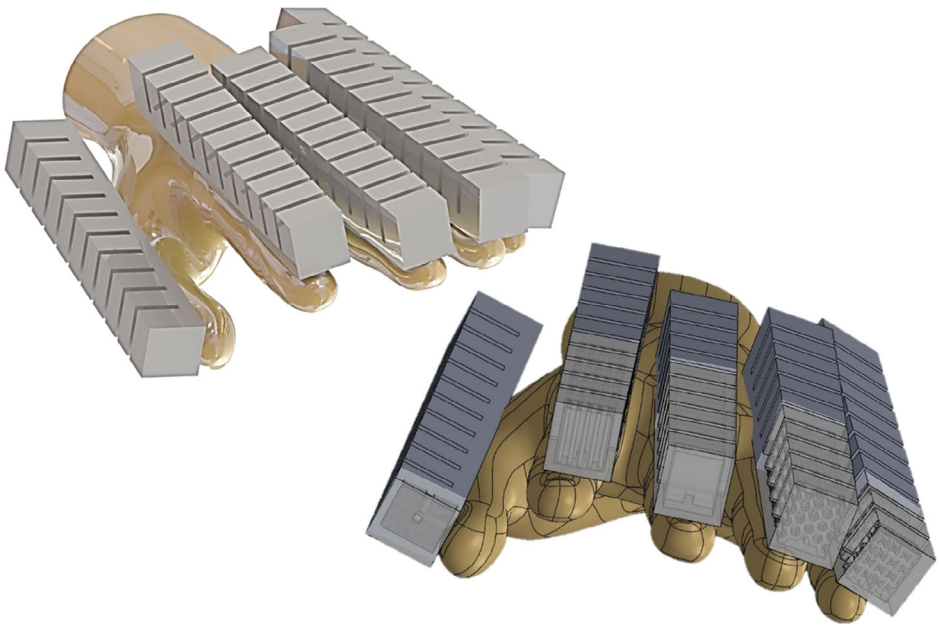

Figure 10. 3D modeling of actuators as a rehabilitative device.

© 2022 The Authors. Advanced Engineering Materials published by Wiley-VCH GmbH

15272648, 0, Downloaded from https://onlinelibrary.wiley.com/doi/10.1002/adem.202200797 by Test, Wiley Online Library on [20/01/2023]. See the Terms and Conditions (https://onlinelibrary.wiley.com/terms-and-conditions) on Wiley Online Library for rules of use; OA articles are governed by the applicable Creative Commons License

4. Conclusion

This article presented a novel class of SPAs inspired by a natural straw and designed for direct FDM 3D printing. A foaming agent varioShore TPU was investigated to find out the material properties and shore hardness. Shore hardnesses A in the range of 60 to 75 were obtained. It was found that nozzle temperature and material flow had a great effect on the shore hardness. The softest value of hardness was achieved using a 220 °C extruder temperature and 60% material flow. FEM was utilized to model the bending and tip force after the TPU material properties were obtained by uniaxial material testing. Bio-inspired lattice structures were designed inside the chambers of the SPAs to evaluate their performance for induced bending angle and blocked force. Auxetic, columns, face-centered cubic, honeycomb, isotruss, oct vertex centroid, and square honeycomb structures were also investigated and analyzed. The experimental trials were conducted by the development of a closed-loop electro-pneumatic board capable of controlling the air input. The measured bending angles and blocked forces were achieved using sensors. Numerical simulations were also conducted to make a comparison with the experimental results to provide further confidence for the theoretical reliability of the obtained data. Lattice structures could improve the pneumatic actuators to have adjustable bending angles without additional components in the system.

The simulation predictions and experimental measurements for bending angles and induced blocked forces are close to each other in most cases. The TPU actuators were tested at pressures up to 500 kPa and bending angles of up to 200° were achieved. Changes in the chambers and using lattice structures within them had a major impact on the force generation and bending angle. The generated force was also investigated, and a maximum value of 2.1 N was achieved using 500 kPa input pressure for the sample without a lattice structure. Pressure testing was also performed to understand the maximum limit of the actuators in terms of applied internal pressure. Finally, prospective soft robotic applications of 3D-printed actuators as wearable devices were demonstrated. With our suggested concept, the actuators would able to aid finger flexion as well as wrist flexion and extension for wearable applications. This method allows for the creation of variable stiffness and controlling soft actuators using the same input pressure that is extremely customizable and tailored to the users. The methods for evaluating and investigating the proposed actuators as a rehabilitative device could be developed in future research works.

Conflict of Interest

The authors declare no conflict of interest.

Data Availability Statement

The data that support the findings of this study are available in the supplementary material of this article.

Keywords

3D printing, finite element modeling, lattice structures, natural straw, pneumatic actuators, soft robotics, varioShore thermoplastic polyurethane

Received: June 3, 2022
Revised: December 5, 2022
Published online:

[1] F. Hartmann, M. Baumgartner, M. Kaltenbrunner, *Adv. Mater.* **2021**, *33*, 2004413.
[2] D. Rus, M. T. Tolley, *Nature* **2015**, *521*, 467.
[3] M. Lalegani Dezaki, M. Bodaghi, A. Serjouei, S. Afazov, A. Zolfagharian, *Sens. Actuators, A* **2022**, *345*, 113779.
[4] T. George Thuruthel, Y. Ansari, E. Falotico, C. Laschi, *Soft Rob.* **2018**, *5*, 149.
[5] W. Hu, W. Li, G. Alici, in *IEEE/ASME Int. Conf. Advanced Intelligent Mechatronics (AIM)*, IEEE, Piscataway, NJ **2018**, pp. 950–955, https://doi.org/10.1109/AIM.2018.8452456.
[6] S. Terrile, M. Argüelles, A. Barrientos, *Sensors* **2021**, *21*, 3253.
[7] M. S. Xavier, A. J. Fleming, Y. K. Yong, *Adv. Intell. Syst.* **2021**, *3*, 2000187.
[8] C. Tawk, A. Gillett, M. in het Panhuis, G. M. Spinks, G. Alici, *IEEE Trans. Rob.* **2019**, *35*, 1268.
[9] R. Mutlu, G. Alici, *Soft Rob.* **2016**, *3*, 120.
[10] A. Pagoli, F. Chapelle, J. A. Corrales, Y. Mezouar, Y. Lapusta, *IEEE Rob. Autom. Lett.* **2021**, *6*, 7706.
[11] I. Hussain, O. Al-Ketan, F. Renda, M. Malvezzi, D. Prattichizzo, L. Seneviratne, R. K. Abu Al-Rub, D. Gan, *Int. J. Rob. Res.* **2020**, *39*, 1635.
[12] M. Kaur, W. S. Kim, *Adv. Intell. Syst.* **2019**, *1*, 1900019.
[13] A. Zolfagharian, S. Gharaie, J. Gregory, M. Bodaghi, A. Kaynak, S. Nahavandi, *Soft Rob.* **2021**, *9*, 680.
[14] B. W. K. Ang, C.-H. Yeow, *IEEE Rob. Autom. Lett.* **2020**, *5*, 3731.
[15] Y. L. Yap, S. L. Sing, W. Y. Yeong, *Rapid Prototyping J.* **2020**, *26*, 1345.
[16] M. Lalegani Dezaki, M. K. A. Mohd Ariffin, S. Hatami, *Rapid Prototyping J.* **2021**, *27*, 562.
[17] M. Al-Rubaiai, T. Pinto, C. Qian, X. Tan, *Soft Rob.* **2019**, *6*, 318.
[18] P. Awasthi, S. S. Banerjee, *Addit. Manuf.* **2021**, *46*, 102177.
[19] M. Mayyas, *Meccanica* **2022**, *57*, 723.
[20] O. D. Yirmibesoglu, J. Morrow, S. Walker, W. Gosrich, R. Canizares, H. Kim, U. Daalkhaijav, C. Fleming, C. Branyan, Y. Menguc, in *2018 IEEE Int. Conf. Soft Robotics (RoboSoft)*, IEEE, Piscataway, NJ **2018**, pp. 295–302, https://doi.org/10.1109/ROBOSOFT.2018.8404935.
[21] B. A. W. Keong, R. Y. C. Hua, *Adv. Mater. Technol.* **2018**, *3*, 1700172.
[22] L. Li, F. Xie, T. Wang, G. Wang, Y. Tian, T. Jin, Q. Zhang, *Soft Rob.* **2022**, *9*, 1108.
[23] A. Zolfagharian, M. A. P. Mahmud, S. Gharaie, M. Bodaghi, A. Z. Kouzani, A. Kaynak, *Virtual Phys. Prototyping* **2020**, *15*, 373.
[24] H. M. C. M. Anver, R. Mutlu, G. Alici, in: *2017 IEEE Int. Conf. Advanced Intelligent Mechatronics (AIM)*, IEEE, Piscataway, NJ **2017**, pp. 442–447, https://doi.org/10.1109/AIM.2017.8014057.
[25] C. Tawk, R. Mutlu, G. Alici, *Front. Rob. AI* **2022**, *8*, 429.
[26] Y. Yan, C. Cheng, M. Guan, J. Zhang, Y. Wang, *Machines* **2022**, *10*, 173.
[27] L. Rosalia, B. W.-K. Ang, R. C.-H. Yeow, *IEEE Rob. Autom. Lett.* **2018**, *3*, 3489.
[28] J. Ogawa, T. Mori, Y. Watanabe, M. Kawakami, M. N. I. Shiblee, H. Furukawa, *IEEE Rob. Autom. Lett.* **2022**, *7*, 2495.
[29] B. W. K. Ang, C.-H. Yeow, in *2017 IEEE/RSJ Int. Conf. Intelligent Robots and Systems (IROS)*, IEEE, Piscataway, NJ **2017**, pp. 1219–1223, https://doi.org/10.1109/IROS.2017.8202295.

© 2022 The Authors. Advanced Engineering Materials published by Wiley-VCH GmbH

15272648, 0, Downloaded from https://onlinelibrary.wiley.com/doi/10.1002/adem.202200797 by Test, Wiley Online Library on [20/01/2023]. See the Terms and Conditions (https://onlinelibrary.wiley.com/terms-and-conditions) on Wiley Online Library for rules of use; OA articles are governed by the applicable Creative Commons License

[30] C. Tawk, M. in het Panhuis, G. M. Spinks, G. Alici, *Soft Rob.* **2018**, *5*, 685.
[31] W. Hu, G. Alici, *Soft Rob.* **2020**, *7*, 267.
[32] H. K. Yap, H. Y. Ng, C.-H. Yeow, *Soft Rob.* **2016**, *3*, 144.
[33] O. H. Yeoh, *Rubber Chem. Technol.* **1993**, *66*, 754.
[34] L. Marechal, P. Balland, L. Lindenroth, F. Petrou, C. Kontovounisios, F. Bello, *Soft Rob.* **2021**, *8*, 284.
[35] L. P. Hyatt, R. L. Harne, *Adv. Eng. Mater.* **2022**, *24*, 2101375.
[36] P. Huang, F. Wu, B. Shen, X. Ma, Y. Zhao, M. Wu, J. Wang, Z. Liu, H. Luo, W. Zheng, *Chem. Eng. J.* **2019**, *370*, 1322.
[37] A. R. Damanpack, A. Sousa, M. Bodaghi, *Micromachines* **2021**, *12*, 866.
[38] W. Hu, R. Mutlu, W. Li, G. Alici, *Robotics* **2018**, *7*, 24.
[39] P. Moseley, J. M. Florez, H. A. Sonar, G. Agarwal, W. Curtin, J. Paik, *Adv. Eng. Mater.* **2016**, *18*, 978.
[40] M. S. Xavier, C. D. Tawk, Y. K. Yong, A. J. Fleming, *Sens. Actuators, A* **2021**, *332*, 113199.
[41] W. Huang, Z. Xu, J. Xiao, W. Hu, H. Huang, F. Zhou, *IEEE Access* **2020**, *8*, 193827.
[42] P. Polygerinos, N. Correll, S. A. Morin, B. Mosadegh, C. D. Onal, K. Petersen, M. Cianchetti, M. T. Tolley, R. F. Shepherd, *Adv. Eng. Mater.* **2017**, *19*, 1700016.
[43] T. Wienzek, A. Seibel, *Adv. Eng. Mater.* **2019**, *21*, 1801200.
[44] L. Y. W. Loh, U. Gupta, Y. Wang, C. C. Foo, J. Zhu, W. F. Lu, *Adv. Eng. Mater.* **2021**, *23*, 2001082.
[45] H. K. Yap, J. H. Lim, F. Nasrallah, J. C. H. Goh, R. C. H. Yeow, in *2015 IEEE Int. Conf. on Robotics and Automation (ICRA)*, IEEE, Piscataway, NJ **2015**, pp. 4967–4972, https://doi.org/10.1109/ICRA.2015.7139889.
[46] J. C. Yeo, H. K. Yap, W. Xi, Z. Wang, C.-H. Yeow, C. T. Lim, *Adv. Mater. Technol.* **2016**, *1*, 1600018.
[47] H. K. Yap, B. W. K. Ang, J. H. Lim, J. C. H. Goh, C.-H. Yeow, in *2016 IEEE Int. Conf. Robotics and Automation (ICRA)*, IEEE, Piscataway, NJ **2016**, pp. 3537–3542, https://doi.org/10.1109/ICRA.2016.7487535.
[48] G. Alici, T. Canty, R. Mutlu, W. Hu, V. Sencadas, *Soft Rob.* **2018**, *5*, 24.

© 2022 The Authors. Advanced Engineering Materials published by Wiley-VCH GmbH

15272648, 0, Downloaded from https://onlinelibrary.wiley.com/doi/10.1002/adem.202200797 by Test, Wiley Online Library on [20/01/2023]. See the Terms and Conditions (https://onlinelibrary.wiley.com/terms-and-conditions) on Wiley Online Library for rules of use; OA articles are governed by the applicable Creative Commons License